



## Intraband Lifshitz transition and Stoner ferromagnetism in Janus $PA_2As$ ( $A = Si, Ge, Sn, \text{ and } Pb$ ) monolayers

Ming-Yang Liu <sup>1</sup>, Long Gong,<sup>1</sup> Yao He <sup>1,\*</sup>, and Chao Cao<sup>2</sup>

<sup>1</sup>*Department of Physics, Yunnan University, Kunming 650091, China*

<sup>2</sup>*Department of Physics, Hangzhou Normal University, Hangzhou 310036, China*



(Received 15 April 2021; revised 26 June 2021; accepted 29 June 2021; published 9 July 2021)

Using first-principles calculations, a class of Janus two-dimensional materials,  $PA_2As$  ( $A = Si, Ge, Sn, \text{ and } Pb$ ) monolayers, is predicted to be dynamically and thermally stable. The band gap of  $PA_2As$  can be linearly modulated by external strain and electric field. The presence of the peculiar sombrero-type band in strained  $PA_2As$  results in the intraband Lifshitz transition near the valence band top when including Rashba spin-orbit coupling. The energy range of intraband Lifshitz transition is linearly dependent on electric field, indicating potential electric control of the Fermi surface properties. In particular, hole doping leads to the ferromagnetic transition in  $PA_2As$  due to Van Hove singularity and a divergence with  $1/\sqrt{E}$  of the density of states. This ferromagnetism can be understood in terms of the Stoner criterion  $D(E_F)I_S > 1$ . A saturated magnetic moment of  $1 \mu_B/\text{hole}$  is obtained in hole-doped  $PSn_2As$  and  $PPb_2As$  with a wide range of hole densities. The highest Curie transition temperature  $T_c$  is estimated to be 93.5 K at the mean field level. We demonstrate that hole density and tensile strain are two effective approaches to control the Stoner ferromagnetism in practical applications. Moreover, various electronic transitions, such as semiconductor to half-metal, half-metal to metal, and semiconductor to metal, are revealed in hole-doped  $PA_2As$ . Finally, we explore the feasibility of realizing ferromagnetism by introducing  $p$ -type dopants and defects. The experimentally controlled intraband Lifshitz transition and Stoner ferromagnetism demonstrate that Janus  $PA_2As$  monolayers have a wide application potential in future electronic and spintronic devices.

DOI: [10.1103/PhysRevB.104.035409](https://doi.org/10.1103/PhysRevB.104.035409)

### I. INTRODUCTION

Due to a cornucopia of intriguing properties in low-dimensional materials, the study of two-dimensional (2D) materials has become one of the most attractive fields in condensed matter physics [1–3]. In view of potential applications in next-generation electronic and spintronic devices, 2D materials with outstanding electronic and magnetic properties are more favorable. Therefore, there has been a surge of effort in exploring tunable electronic and magnetic properties in certain 2D materials [4–8]. Although the electronic properties, in general, are easy to modulate, the controlled magnetism in nonmagnetic 2D materials has been a challenge [9]. To achieve magnetism in nonmagnetic 2D materials, introduction of external approaches such as doping atoms [4,10–12] and defects [13–15] is the common strategy in theoretical study so far. However, the magnetism achieved by these approaches has been difficult to modulate and control in practical experiment [9]. Thus, it is a significant issue to explore the experimentally controlled magnetism in certain 2D materials.

Recently, a class of 2D materials with a peculiar valence band top (VBT) has received tremendous interest in the exploration of inherent ferromagnetism [9,16–19]. Owing to the presence of saddle points of energy dispersion in  $\mathbf{k}$  space, the sombrero-type band forms near the VBT, which gives rise to

fascinating characteristics of the density of states (DOS), such as a Van Hove singularity diverging with  $1/\sqrt{E}$  [16,20]. The sombrero-type band can be described analytically by  $E(k) = Ak^4 + Bk^2 + E_0$ , where  $E_0$  is defined as the sombrero depth. At  $E = E_0$ , DOS shows the second Van Hove singularity with a step function discontinuity. When the sombrero-type band is the valence band edge, the  $A$  and  $B$  constants are  $A < 0$  and  $B > 0$  [16]. This unusual electronic structure often results in electronic instability, emerging ferromagnetic transition [9,16], superconductivity [21], and density waves [20]. In particular, inherent ferromagnetism has been achieved by injecting hole carriers [9,16], and thus it can be tuned effectively through doping carrier density [9,16,22,23] and external strain [24], as well as the number of layers [25]. Up to now, many 2D materials have been predicted to host the sombrero-type band near the VBT, such as metal monochalcogenide (GaS, GaSe, GaO, and InO) [9,26],  $\alpha$ -SnO [16,18],  $InP_3$  [27], strained phosphorene [24], and others. All of these 2D monolayers exhibit tunable ferromagnetism and half-metallicity, demonstrating that the ferromagnetic transition is general for 2D materials with the sombrero-type VBT. Due to the ultrathin character of 2D materials, high doping density has been reported in graphene of the order of  $10^{14} \text{ cm}^{-2}$  [28] and in transition metal dichalcogenide of the order of  $10^{13} \text{ cm}^{-2}$  [29] by gating techniques. Compared to introducing external approaches, carrier doping via gating techniques is more experimentally feasible. These studies strongly suggest that 2D materials with the sombrero-type band offer a possible

\*Corresponding author: [yhe@ynu.edu.cn](mailto:yhe@ynu.edu.cn)

opportunity to realize the experimentally controllable ferromagnetism.

On the other hand, the introduction of mirror symmetry breaking in 2D materials can lead to some spin-related properties, especially with the sombrero-type band. For instance, InSe bilayer and Janus  $X\text{Sn}_2Y$  monolayers ( $X$  and  $Y$  are the group V elements) have been proposed theoretically as potential candidates to probe spin-charge conversion (also referred to as the inverse Edelstein effect) and intraband Lifshitz transition [30,31]. They are recognized to have predominant promise for future electronic and spintronic devices. There has not been much reported on simultaneous intraband Lifshitz transition and hole doping induced ferromagnetism in certain 2D materials. With this in mind, it may be imperative to discuss this issue. Very recently,  $AX$  ( $A$  and  $X$  are the group IV and V elements, respectively) 2D monolayers with metal monochalcogenide structure have been predicted to be dynamically and thermally stable [32–34]. Among them, AP and AAs monolayers have the sombrero-type band or a small energy difference between the  $\sigma$  and  $\pi$  bonding levels near the VBT, and the four-sublayer structure provides a possibility for constructing Janus 2D materials. Therefore, AP and AAs monolayers forming the Janus structure will be possible prototypes to investigate intraband Lifshitz transition and inherent ferromagnetism in 2D materials.

In this work, we predict, through first-principles calculations, a class of stable Janus 2D materials,  $\text{PA}_2\text{As}$  ( $A = \text{Si}, \text{Ge}, \text{Sn}, \text{and Pb}$ ) monolayers. Their electronic properties are linearly tunable via external strain and electric field. Particularly, the semiconductor-metal transition is found in  $\text{PPb}_2\text{As}$  under both compressive and tensile strain. Due to the presence of the peculiar sombrero-type VBT, an intriguing intraband Lifshitz transition is revealed in the strained  $\text{PA}_2\text{As}$ . The Rashba effect leads to a perfect linear relation between the first Lifshitz transition range and external electric field. Furthermore, the sombrero-type band induced Van Hove singularity of the DOS offers an opportunity to explore the Stoner ferromagnetic transition in the hole-doped  $\text{PA}_2\text{As}$ . It has been found that the magnetism can be tuned effectively through hole density and tensile strain. We unveil not only the ferromagnetic transition, but also the electronic transition upon hole doping, such as semiconductor to half-metal, half-metal to metal, and semiconductor to metal. Our results demonstrate that Janus  $\text{PA}_2\text{As}$  monolayers are promising candidates for the future electronic and spintronic devices owing to the experimentally controllable intraband Lifshitz transition and Stoner ferromagnetism.

## II. COMPUTATIONAL METHODS

All first-principles calculations were performed using the Perdew-Burke-Ernzerhof (PBE) exchange-correlation functional within the generalized gradient approximation (GGA) as implemented in the Vienna *ab initio* simulation package (VASP) [35–37]. The electronic band structure was also checked under the screened hybrid functional method in the HSE06 level [38]. Both without and with spin-orbit coupling (SOC) were included in the PBE and HSE06 levels for the electronic band structure calculations. The kinetic energy cutoff for the plane-wave basis was set to be 500 eV. All atoms were relaxed until an energy convergence of  $10^{-6}$  eV,

forcing convergence of  $0.01 \text{ eV}/\text{\AA}$ . The first Brillouin-zone integration was carried out using an  $11 \times 11 \times 1\Gamma$ -point centered  $k$ -point grid for structure optimization; it was improved to  $17 \times 17 \times 1$  for self-consistent calculations. In the carrier doping calculations, the hole doping was realized by removing the total number of electrons in the unit cell and a jellium background with the opposite charge was introduced. To converge the magnetic state, we tested different  $k$ -point grids of  $17 \times 17 \times 1$ ,  $21 \times 21 \times 1$ ,  $31 \times 31 \times 1$ ,  $41 \times 41 \times 1$ , and  $50 \times 50 \times 1$  in spin-polarization calculations. It found that a  $k$ -point grid of  $17 \times 17 \times 1$  was enough to obtain a stable magnetic state. The  $p$ -type dopants and vacancy defect calculations were performed to check the predicted magnetic state, which was within the  $4 \times 4 \times 1$  supercell geometry model. A vacuum layer of  $20 \text{ \AA}$  was used to eliminate the interaction between adjacent slabs.

The dynamical stability of  $\text{PA}_2\text{As}$  was confirmed by performing the phonon dispersion calculation as implemented in the QUANTUM ESPRESSO code [39]. The thermal stability was tested by *ab initio* molecular dynamics (AIMD) simulations within a  $4 \times 4 \times 1$  supercell at the temperature of 300 K. The total simulation time was 3 ps with a time step of 3 fs. The mechanical properties and effective masses were calculated by the VASP code [40]. Analysis of the charge transfers was determined by the Bader techniques [41]. The Fermi surface and Berry curvature properties were calculated by using the WANNIERTOOLS code [42] based on the tight-binding (TB) model with the maximally localized Wannier functions (MLWFs) [43]. MLWFs were constructed by using the software package WANNIER90 [44] with interfacing VASP.

## III. RESULTS AND DISCUSSION

### A. Structure stability, mechanical properties, and polarization effect

We begin by describing the structural properties to understand the Janus construction.  $AX$  2D monolayers have a  $D_{3h}$  symmetry group, similar to the metal monochalcogenide. The mirror symmetry breaking can be introduced via replacing group V atoms on the same side with different group V atoms. Thus, both AP and AAs can form ternary Janus  $\text{PA}_2\text{As}$  monolayers with a  $C_{3v}$  symmetry group, as shown in Fig. 1(a). The unit cell of Janus  $\text{PA}_2\text{As}$  monolayers belongs to the hexagonal symmetry and is composed of one P atom, one As atom, and two A atoms, in which two A atomic layers are sandwiched by P and As atomic layers. The optimized lattice constants are listed in Table I and the total energies with the lattice constants are plotted in Fig. S1 in the Supplemental Material [45]. The lattice constants ( $a = b$ ) of  $\text{PA}_2\text{As}$  increase with the atomic number of the A atoms as expected. Both the lattice constants and layer thicknesses ( $d$ ) are the average value of those of AP and AAs monolayers. Compared to their binary counterparts AP and AAs, the alteration of the lattice constants of  $\text{PA}_2\text{As}$  produces a lattice strain on two atomic surfaces. Using the lattice constant of  $\text{PA}_2\text{As}$  as a reference, the P atomic surface is exposed to the tensile strain while the As atomic surface is exposed to the compressive strain. As we will see later, this inherent lattice strain plays an important role in determining the difference of electronic structure between  $\text{PA}_2\text{As}$  and their

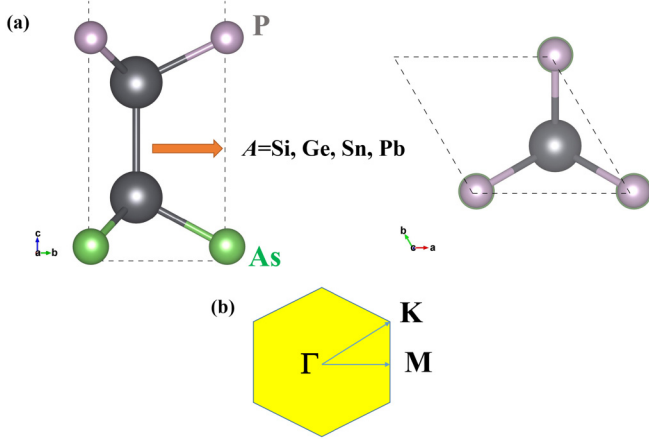


FIG. 1. (a) Side and top views of Janus  $PA_2As$  monolayers; the black balls represent the group IV elements Si, Ge, Sn, and Pb. (b) The first Brillouin zone and high-symmetry points in the reciprocal space.

binary counterparts. In a similar manner,  $A$ -P bond length ( $L_1$ ),  $A$ -As bond length ( $L_2$ ),  $A$ -A bond length ( $L_3$ ), and P-As distance ( $d$ ) also increase with the atomic number of the  $A$  atoms, as summarized in Table I.

The energy feasibility of Janus  $PA_2As$  monolayers can be checked by calculating the formation enthalpy  $E_{\text{for}}$  with the expression as follows:

$$E_{\text{for}} = [E_{\text{tot}} - (n_1 E_P + n_2 E_{As} + n_3 E_A)] / (n_1 + n_2 + n_3), \quad (1)$$

where  $E_{\text{tot}}$  is the total ground state energy of the unit cell;  $E_P$ ,  $E_{As}$ , and  $E_A$  are the chemical potential of isolated P, As, and A atoms, respectively.  $n_1$ ,  $n_2$ , and  $n_3$  are the number of P, As, and A atoms in the unit cell, respectively. According to the definition of  $E_{\text{for}}$ , the negative value confirms the energy feasibility of  $PA_2As$ . As compared to their binary counterparts, Janus  $PA_2As$  becomes more energetically feasible, for which forming the  $PSi_2As$  is the most exothermic process due to the strong electronegativity of Si. It should be mentioned that  $E_{\text{for}}$  of  $PSn_2As$  predicted here is larger than that

of our previous work [31] due to include the spin polarization in calculating the chemical potential of an isolated atom in Ref. [31]. The dynamical stability of  $PA_2As$  is checked by calculating the phonon spectrum (see Fig. S2 [45]). No imaginary frequency of the phonon spectrum in all Janus  $PA_2As$  monolayers confirms their dynamical stabilities. Although the phonon spectrum ensures the dynamical stability at the ground state, they may be unstable at finite temperature. Thus, examining the thermal stability of  $PA_2As$  at finite temperature is needed. Our AIMD simulations demonstrate that the structure of  $PA_2As$  is hardly affected after the simulations (see Fig. S3 [45]), verifying the thermal stability at room temperature.

For a predicted class of Janus monolayers, the mechanical properties are essential for their practical applications. They can be obtained from calculating the elastic constants  $C_{ij}$  which are evaluated from the strain-energy curve [46]. The calculated elastic constants  $C_{ij}$  are listed in Table II. First, we check the Born-Huang stability criteria:  $C_{11} > |C_{12}|$ ,  $C_{22} > 0$ ,  $C_{66} > 0$ ,  $C_{11}C_{22} - C_{12}^2 > 0$ . It is clear that all  $PA_2As$  monolayers satisfy the Born-Huang stability criteria. Second, on the basis of the calculated elastic constants, the mechanical properties, such as the 2D layer modulus  $\gamma^{2D} = \frac{1}{2}(C_{11} + C_{12})$ , Young's modulus  $Y_{2D} = [C_{11}^2 - C_{12}^2]/C_{11}$ , and Poisson's ratio  $\nu = C_{12}/C_{11}$ , are derived [47]. The 2D layer modulus and Young's modulus decrease with the atomic number of the  $A$  atoms, suggesting that the elongation of the lattice constant lowers the in-plane stiffness, as well as weakens the resistance to stretching. In contrast to predicted GaS and GaSe monolayers [48],  $PSi_2As$  and  $PGe_2As$  have larger in-plane stiffness, whereas  $PSn_2As$  and  $PPb_2As$  have smaller in-plane stiffness. Although the Poisson's ratio increases with the atomic number of the  $A$  atoms from  $PSi_2As$  to  $PSn_2As$ , it still is smaller than 1/3, indicating a brittle character based on the Frantsevich rule [49]. Distinct from other types of  $PA_2As$ , the  $\nu$  of  $PPb_2As$  is larger than 1/3, which originates from the metallic character of Pb. Besides, we notice that these mechanical quantities are smaller than those of reported  $HfN_2$  and  $WSe_2$  monolayers [47]. A recent study also predicted a class of Janus 2D materials [50], in which the evaluated mechanical properties of  $PSi_2As$  are comparable to our present results.

TABLE I. Calculated structural properties of Janus  $PA_2As$  monolayers: lattice constant  $a = b$ ,  $A$ -P bond length  $L_1$ ,  $A$ -As bond length  $L_2$ ,  $A$ -A bond length  $L_3$ , layer thickness (namely, the distance between P and As)  $d$ , formation enthalpy  $E_{\text{for}}$ , charge transfer of A-As atomic group  $\Delta q$ , work function difference between two sides  $\Delta\phi$ , and dipole moment  $\mu$ . Among these, the structural parameters of the  $AX$  monolayer are cited from Ref. [32].

Structure	$a = b$ (Å)	$L_1$ (Å)	$L_2$ (Å)	$L_3$ (Å)	$d$ (Å)	$E_{\text{for}}$ (eV/atom)	$\Delta q$ ( $e$ )	$\Delta\phi$ (eV)	$\mu$ (D)
$PSi_2As$	3.61	2.30	2.37	2.37	4.49	-4.51	0.047	0.280	0.086
$PGe_2As$	3.74	2.40	2.46	2.50	4.72	-3.94	0.034	0.297	0.104
$PSn_2As$	4.02	2.58	2.65	2.88	5.29	-3.56	0.060	0.268	0.102
$PPb_2As$	4.18	2.69	2.75	3.05	5.55	-3.16	0.023	0.274	0.115
SiP	3.53	2.28	-	2.37	4.41	-4.19	-	-	-
SiAs	3.70	-	2.40	2.36	4.57	-3.85	-	-	-
GeP	3.66	2.37	-	2.51	4.65	-3.60	-	-	-
GeAs	3.82	-	2.49	2.50	4.80	-3.36	-	-	-
SnP	3.95	2.56	-	2.89	5.22	-3.28	-	-	-
SnAs	4.09	-	2.67	2.88	5.37	-3.10	-	-	-
PbP	4.12	2.67	-	3.06	5.49	-2.83	-	-	-
PbAs	4.25	-	2.77	3.05	5.62	-2.72	-	-	-

TABLE II. Calculated mechanical properties of Janus PA<sub>2</sub>As monolayers: elastic constants  $C_{ij}$ , 2D layer modulus  $\gamma^{2D}$ , Young's modulus  $Y_{2D}$ , Poisson's ratio  $\nu$ .

Structure	$C_{11} = C_{22}$ (N/m)	$C_{12}$ (N/m)	$C_{66}$ (N/m)	$\gamma^{2D}$ (N/m)	$Y_{2D}$ (N/m)	$\nu$ (N/m)
PSi <sub>2</sub> As	121.73	23.35	49.19	72.54	117.25	0.19
PGe <sub>2</sub> As	101.65	21.13	40.26	61.39	97.25	0.21
PSn <sub>2</sub> As	77.11	18.70	29.20	47.90	72.57	0.24
PPb <sub>2</sub> As	54.13	18.04	18.04	36.08	48.12	0.33

In Janus structure, intrinsic mirror symmetry breaking is responsible for the polarization effect. Generally, the polarization effect of Janus 2D materials can result in internal electric-field, dipole moment, and surface work function difference [51–53]. In order to more clearly present the origin of the polarization effect, we divide the four-sublayer structure of PA<sub>2</sub>As into two atomic groups, e.g., an A-P group and an A-As group. These two atomic groups are covalently bonded by two A atoms, as depicted by the electron localization function (see Fig. S4 [45]). Because of the strong metallicity of the Pb atom, the weakest covalent bond of two atomic groups is found in PPb<sub>2</sub>As. Bader charge analysis suggests that for all PA<sub>2</sub>As monolayers, the charge is transferred between two atomic groups even though both P and As atoms receive charge from the A atoms. The calculated total charge transfer  $\Delta q$  of the A-As atomic group is listed in Table I. Positive  $\Delta q$  indicates the charge denoted by the A-As atomic group, through which the net internal electric field is formed with the direction pointing from As to P. Moreover, the work function change is another indicator of the presence of the internal electric field. This can be seen from the planar average of the electrostatic potential shown in Fig. S5 [45]. It is found that the work function of the As side is lower than that of the P side in all PA<sub>2</sub>As monolayers, agreeing with the charge transfer analysis above. The calculated nonzero dipole  $\mu$  further confirms the presence of the polarization effect in Janus PA<sub>2</sub>As monolayers. These dipoles are comparable to those of Janus XSn<sub>2</sub>Y monolayers but are smaller than those of Janus transition metal dichalcogenide [31,52].

### B. Strain and electric-field effects on the electronic properties

The orbital projected band structures of Janus PA<sub>2</sub>As monolayers without SOC are shown in Fig. 2. Both PSi<sub>2</sub>As and PGe<sub>2</sub>As are the indirect band gaps with the conduction band bottom (CBB) locating at the  $M$  point and the VBT locating at the  $\Gamma$  point. Particularly, both the CBB and VBT of PSn<sub>2</sub>As reside at the  $\Gamma$  point, exhibiting the direct band gap feature. PPb<sub>2</sub>As is also the indirect band gap, but its VBT is along the  $\Gamma$ - $K$  line owing to the sombrero-type band. The peculiar dispersion of PPb<sub>2</sub>As yields the highly localized DOS near the VBT showing a sharp Van Hove singularity (see Fig. S6 [45]). The calculated band gaps of PA<sub>2</sub>As are summarized in Table III. The inherent lattice strain significantly affects the band gaps of PA<sub>2</sub>As, as compared to their binary counterparts. For example, the band gap of PSi<sub>2</sub>As is smaller than that of SiP and SiAs since the P atomic surface is stretched and the As atomic surface is compressed. The calculated carrier effective masses of PA<sub>2</sub>As along two different  $k$  directions are summarized in Table III. When the CBB locates at the  $M$  point, the

electron effective mass  $m_{\text{CBB}}^*$  shows evident anisotropy, but it shows isotropy when the CBB locates at the  $\Gamma$  point. The hole effective mass  $m_{\text{VBT}}^*$  has a slight difference between two high-symmetry directions.

Orbital projection analyses reveal that for PSi<sub>2</sub>As, PGe<sub>2</sub>As, and PSn<sub>2</sub>As, the VBT is contributed by the hybridized As- and  $A$ - $p_{xy}$  orbitals, but for PPb<sub>2</sub>As the VBT is composed of the hybridized P-, As-, and  $A$ - $p_z$  orbitals. In addition, the characteristics of the frontier states are used to gain insight into the electronic properties near the VBT, which can be captured by calculating the partial charge density (see Fig. S7 [45]). The frontier states of PSi<sub>2</sub>As and PGe<sub>2</sub>As are controlled by As and A atoms, displaying the  $\sigma$ -type bond. However, P, As, and A atoms contribute the frontier states in PSn<sub>2</sub>As and PPb<sub>2</sub>As, displaying the  $\pi$ -type bond. This  $\pi$ -type bonding character is associated with the sombrero-type band. Although the sombrero-type VBT is not observed in PSi<sub>2</sub>As, PGe<sub>2</sub>As, and PSn<sub>2</sub>As, the presence of a small energy difference between the  $\sigma$ -type and  $\pi$ -type levels provides a potential advantage to change the characteristics of the frontier states via external strain, particularly for PSn<sub>2</sub>As. In the subsequent discussion, we will show how the changes of frontier states effectively

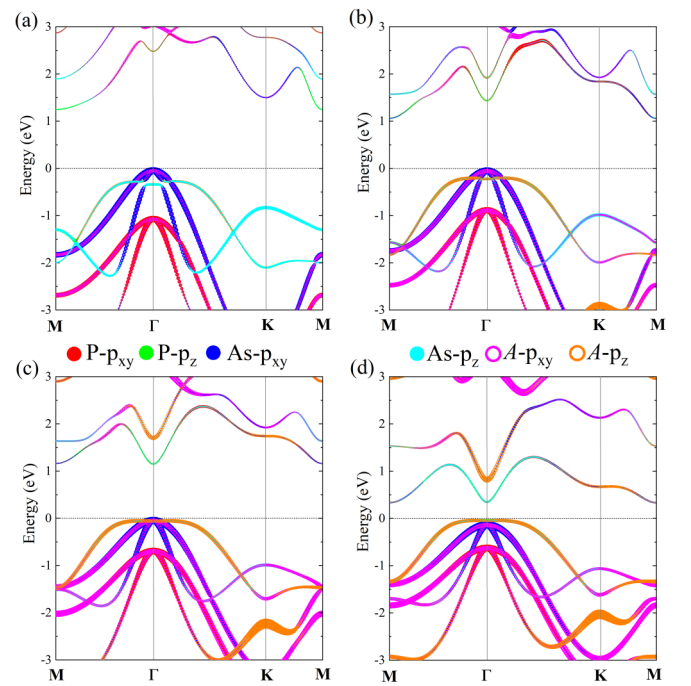


FIG. 2. Orbital projected band structures of Janus PA<sub>2</sub>As monolayers without SOC; the size of the circle is proportional to the orbital weight. The Fermi level is set at the zero energy.



TABLE III. Calculated electronic properties of Janus  $PA_2As$  monolayers. PBE band gap without and with SOC:  $E_{g-PBE}$  and  $E_{g-PBE+SOC}$ . HSE06 band gap without and with SOC:  $E_{g-HSE}$  and  $E_{g-HSE+SOC}$ . Carrier effective mass of CBB along two high-symmetry directions:  $m_{CBB1}^*$  and  $m_{CBB2}^*$ . Carrier effective mass of VBT along two high-symmetry directions:  $m_{VBT1}^*$  and  $m_{VBT2}^*$ . Among these, the band gaps of the AX monolayer are cited from Ref. [32].

Structure	$E_{g-PBE}$ (eV)	$E_{g-PBE+SOC}$ (eV)	$E_{g-HSE}$ (eV)	$E_{g-HSE+SOC}$ (eV)	$m_{CBB1}^*$ ( $ m^*/m_0 $ )	$m_{CBB2}^*$ ( $ m^*/m_0 $ )	$m_{VBT1}^*$ ( $ m^*/m_0 $ )	$m_{VBT2}^*$ ( $ m^*/m_0 $ )
PSi <sub>2</sub> As	1.29	1.21	1.95	1.85	0.146	1.759	0.505	0.521
PGe <sub>2</sub> As	1.11	1.00	1.76	1.65	0.251	0.626	0.527	0.549
PSn <sub>2</sub> As	1.19	1.06	1.78	1.65	0.155	0.155	1.411	1.437
PPb <sub>2</sub> As	0.38	0.28	0.72	0.56	0.251	0.626	3.182	3.379
SiP	1.52	1.51	2.22	–	–	–	–	–
SiAs	1.63	1.54	2.27	–	–	–	–	–
GeP	1.35	1.34	2.05	–	–	–	–	–
GeAs	1.20	1.08	1.81	–	–	–	–	–
SnP	1.29	1.28	1.91	–	–	–	–	–
SnAs	1.14	1.05	1.72	–	–	–	–	–
PbP	0.40	0.38	0.76	–	–	–	–	–
PbAs	0.36	0.25	0.67	–	–	–	–	–

modulate intraband Lifshitz transition and hole doping induced ferromagnetism.

Moreover, an important issue of why only PPb<sub>2</sub>As has the sombrero-type VBT can be explained on the basis of the inherent lattice strain. For AP and AAs monolayers, SiP has the sombrero-type VBT, whereas SiAs has the parabolic-type VBT. Upon formation of PSi<sub>2</sub>As, the energy difference between the  $\sigma$ -type and  $\pi$ -type levels is enlarged because of the As atomic surface compressed by the lattice strain. As a result, PSi<sub>2</sub>As cannot form the sombrero-type VBT. A similar situation is found in PGe<sub>2</sub>As. Although SnAs has the sombrero-type VBT, forming the PSn<sub>2</sub>As results in the  $\sigma$ -type level being higher than the  $\pi$ -type level since the As atomic surface is compressed by the lattice strain. Thus, the sombrero-type VBT disappears in PSn<sub>2</sub>As. For PbAs, a large energy difference between the  $\sigma$ -type and  $\pi$ -type levels enables the sombrero-type VBT to remain in PPb<sub>2</sub>As. Similar analyses have also been clarified in the Janus In<sub>2</sub>SSe monolayer [54], in which the inherent lattice strain removed the sombrero-type VBT of InS and InSe.

In the presence of SOC, as seen in Table III, the band gaps of  $PA_2As$  decrease by  $\sim 0.1$  eV. The dramatic effect of SOC on the band structure is noticed in PPb<sub>2</sub>As (see Fig. S8 [45]). For instance, the Rashba-type spin splitting is found at the CBB, which is caused by the intrinsic mirror symmetry breaking of the Janus structure. The estimated Rashba parameter  $\alpha_R$  is 7.53 eV Å obtained by using the expression  $\alpha_R = 2E_R/k_R$  based on the linear Rashba model [31]. This value is larger than that of the predicted Rashba 2D materials [52]. Interestingly, an additional Rashba-type spin splitting emerges from the second CBB at the  $\Gamma$  point. That is to say, PPb<sub>2</sub>As shows the double Rashba effects at the  $\Gamma$  point. The second Rashba parameter  $\alpha_R$  is estimated to be 3.23 eV Å. This interesting result is also reported in the Janus  $XSn_2Y$  monolayers [31]. For PSn<sub>2</sub>As, weak SOC gives rise to a small Rashba parameter  $\alpha_R$  of 0.8 eV Å. However, the Rashba-type spin splitting is absent in PSi<sub>2</sub>As and PGe<sub>2</sub>As. In addition, all Janus  $PA_2As$  monolayers have a circle-type Fermi surface (see Fig. S9 [45]). We notice that the Fermi surface topology of PSn<sub>2</sub>As and PPb<sub>2</sub>As is different from that of PGe<sub>2</sub>As and PSi<sub>2</sub>As since

the sombrero-type band of PSn<sub>2</sub>As and PPb<sub>2</sub>As is close to the Fermi level. Considering a small energy difference between the  $\sigma$ -type and  $\pi$ -type levels, the Fermi surface topology of  $PA_2As$  can be modified by external modulation.

The band structures of  $PA_2As$  are checked using the HSE06 hybrid functional (see Fig. S10 [45]), and the obtained band gaps are summarized in Table III. Although the band gaps with SOC increase by 0.64 and 0.65 eV for PSi<sub>2</sub>As and PSn<sub>2</sub>As respectively, the band structure profiles are nearly in line with the PBE functional results. For PSn<sub>2</sub>As and PPb<sub>2</sub>As, the HSE06 level not only widens the band gap but also slightly modifies the band structure. For instance, the VBT of PSn<sub>2</sub>As becomes the sombrero-type band and the CBB shifts to the  $M$  point in the absence of SOC.

Because of the ultrathin character of 2D materials, their physical properties are easily tuned by external modulation. Before investigating the intraband Lifshitz transition and hole doping induced ferromagnetism, it is instructive to consider strain and electric-field effects on the electronic structure. For Janus  $PA_2As$  monolayers, the intrinsic buckling structure and mirror symmetry breaking provide potential advantages to modulate the electronic properties via strain and electric field. These approaches are not only experimentally feasible but also essential to the application of Janus  $PA_2As$  monolayers. In terms of the mechanical properties discussed before, here we consider a small strain range (from  $-5\%$  to  $+5\%$ ). The biaxial strain  $\varepsilon$  that can be denoted by  $\varepsilon = (a - a_0)/a_0 \times 100\%$  is realized by altering the equilibrium lattice constant  $a_0$ . The electric field is simulated by means of the dipole correction method.

As seen in Fig. 3(a), the band gaps of  $PA_2As$  are very sensitive to both compressive and tensile strain. A linear reduction of the band gap with compressive strain is observed in PGe<sub>2</sub>As, PSn<sub>2</sub>As, and PPb<sub>2</sub>As. In particular, the semiconductor-metal transition is found in PPb<sub>2</sub>As when  $\varepsilon > -3\%$ . For tensile strain, the band gap maximum is observed at  $\varepsilon = +1\%$  in PSi<sub>2</sub>As and PGe<sub>2</sub>As but at  $\varepsilon = 0\%$  in PSn<sub>2</sub>As and PPb<sub>2</sub>As, which arises from different band dispersions near the VBT (see Figs. S11–S14 [45]). As expected the sombrero-type VBT emerges in PSi<sub>2</sub>As and PGe<sub>2</sub>As

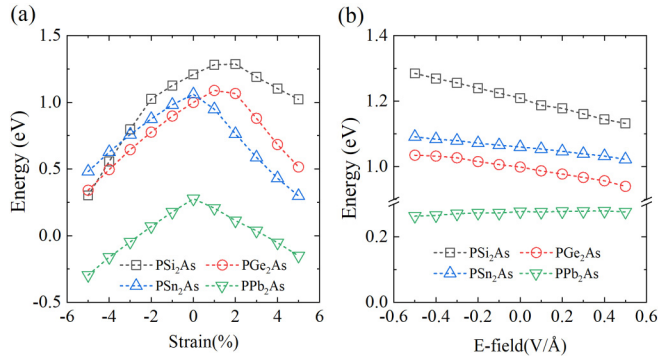


FIG. 3. Band gaps of Janus  $PA_2As$  monolayers as a function of (a) external strain and (b) external electric field.

when  $\varepsilon \geq +2\%$ . Also, the sombrero depth  $E_0$  of  $PSn_2As$  and  $PPb_2As$  increases with tensile strain. These variations would strongly affect the intraband Lifshitz transition and hole-doping effect. For  $PSn_2As$  and  $PPb_2As$ , the band gap decreases linearly with tensile strain. The semiconductor-metal transition is found in  $PPb_2As$  again when  $\varepsilon > +3\%$ .

As discussed before, the presence of intrinsic mirror symmetry breaking produces an internal electric field. Here, the direction of the external electric field is set along the internal electric field. The electric-field dependence of the band gap is plotted in Fig. 3(b). Unlike the strain, the influence of the electric field on the band gap is relatively weak. It is clear that the band gaps of  $PSi_2As$ ,  $PGe_2As$ , and  $PSn_2As$  display a linear reduction within the electric field considered, and the ratios are in accordance with the atomic number of the  $A$  atoms.

Nevertheless, the band gap of  $PPb_2As$  is less influenced. Thus, we can conclude that the smaller the atomic number of the  $A$  atoms, the more tunable the band gap in the external electric field. The reason can be understood qualitatively from the planar average of the electrostatic potential (see Fig. S5 [45]). Because of a large potential difference between the As atomic surface and the P atomic surface in  $PSi_2As$ , its band gap hence is more sensitive to the external electric-field effect. In contrary, a small potential difference leads to the weak electric-field effect on the band gap of  $PPb_2As$ .

### C. Tunable intraband Lifshitz transition of $PA_2As$

The Fermi surface properties are important for the electric transport, nontrivial topology, and superconducting transition [55–58]. The sombrero-type VBT combined with Rashba SOC can result in the intraband Lifshitz transition and inverse Edelstein effect [30]. The Lifshitz transition changes the topology of the Fermi surface, which is crucial for understanding the electronic properties near the Fermi surface. The previous band structure calculations imply the possibility of probing the intraband Lifshitz transition in Janus  $PA_2As$  monolayers. The 2D and 3D band structures of the sombrero-type VBT with SOC are shown in Figs. 4(a) and 4(b). For  $PSi_2As$ ,  $PGe_2As$ , and  $PSn_2As$ , a small energy difference between the V2 and V1 energy levels (two valence band maxima) can be ignored in discussing the intraband Lifshitz transition. For  $PPb_2As$ , however, a relative large energy difference between the V1 and V2 energy levels gives rise to more complicated band dispersion. The intraband Lifshitz transition of  $PPb_2As$  will be discussed separately.

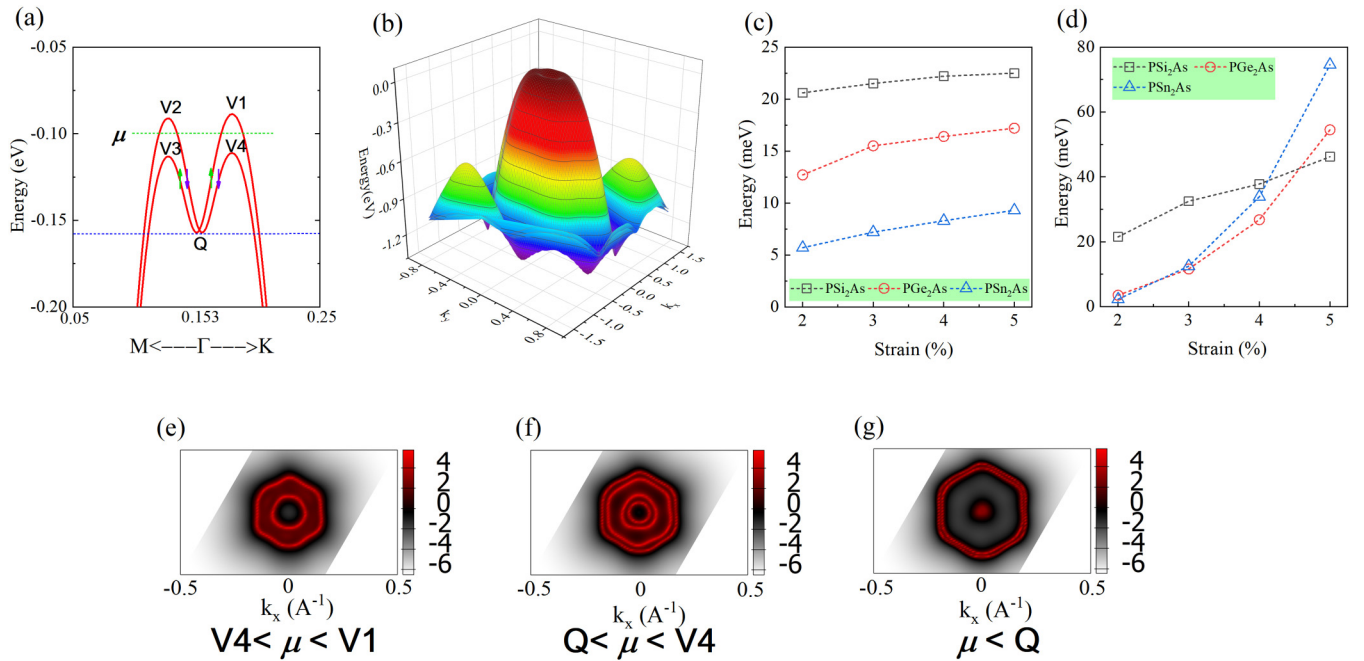


FIG. 4. (a) The sombrero-type band with SOC, in which V1 is the energy level of the VBT, V4 is the first Lifshitz transition point,  $Q$  is the second Lifshitz transition point, and  $\mu$  is the chemical potential. The green and purple arrows denote the spin-up and spin-down channels, respectively. (b) 3D plot of the sombrero band dispersion with SOC. (c) Energy difference  $E_{V1-V4}$  and (d) energy difference  $E_{V4-Q}$  of  $PSi_2As$ ,  $PGe_2As$ , and  $PSn_2As$  as a function of tensile strain. (e)–(g) Fermi surface properties of chemical potential  $\mu$  locates in  $E_{V1-V4}$  ( $V4 < \mu < V1$ ),  $E_{V4-Q}$  ( $Q < \mu < V4$ ), and  $\mu < Q$ , respectively. The color scales represent the weight of the electronic states.

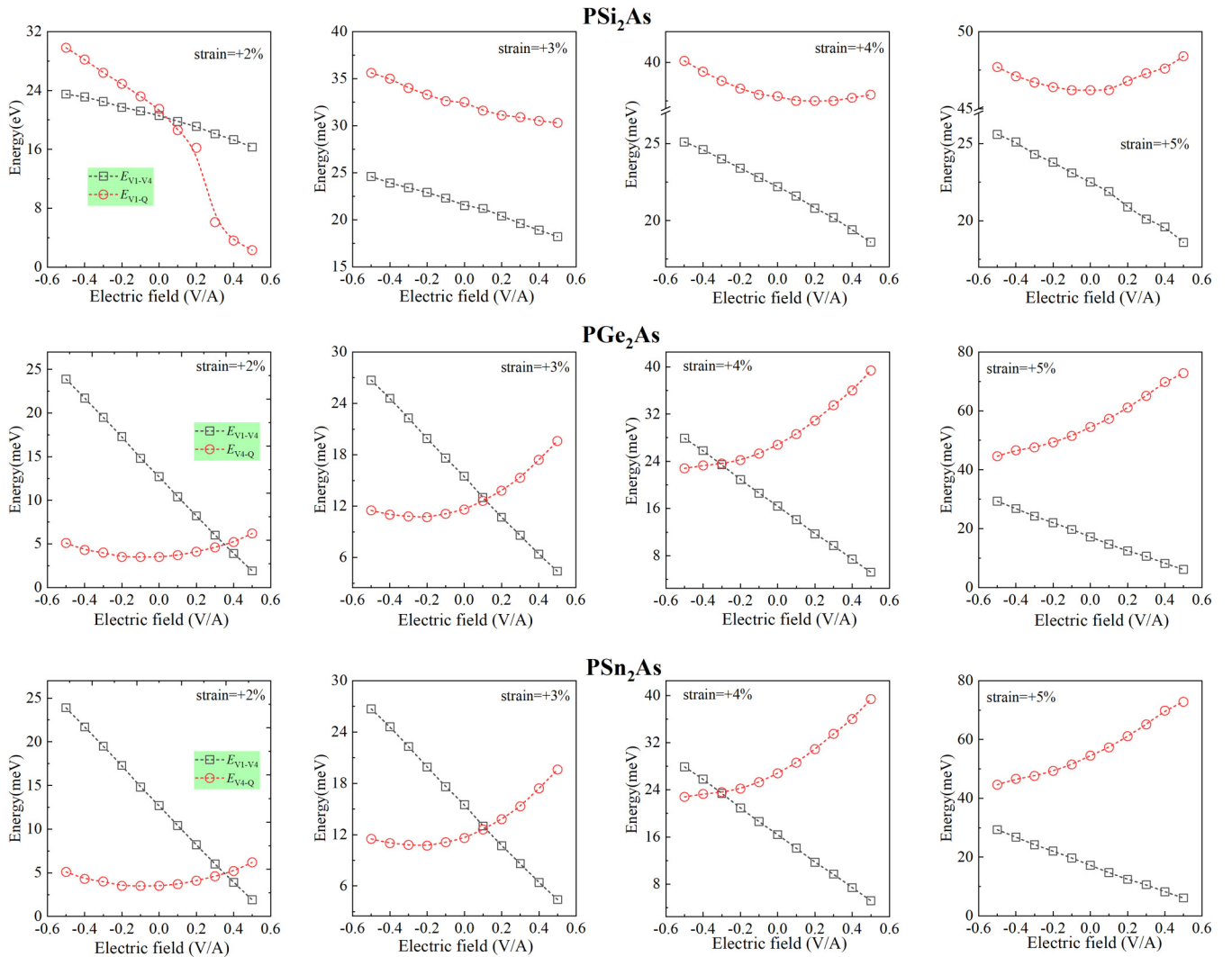


FIG. 5. Energy difference  $E_{V1-V4}$  and  $E_{V4-Q}$  of  $\text{PSi}_2\text{As}$ ,  $\text{PGe}_2\text{As}$ , and  $\text{PSn}_2\text{As}$  under different tensile strains as a function of external electric field.

In Fig. 4(a), an unexpected spin splitting is observed near the VBT, as a result of the combination between the Rashba SOC and the sombrero-type band. It should be mentioned that this spin splitting is different from the general Rashba effect, because there are three different spin textures in the energy ranges  $V1 < E < V4$  ( $E_{V1-V4}$ ),  $V4 < E < Q$  ( $E_{V4-Q}$ ), and  $E < Q$  [30]. We find that  $E_{V1-V4}$  and  $E_{V4-Q}$  can be tuned by tensile strain. As seen in Figs. 4(c) and 4(d), both  $E_{V1-V4}$  and  $E_{V4-Q}$  increase with tensile strain; in particular  $E_{V4-Q}$  is more sensitive to the variation of tensile strain. We then calculate the Fermi surface properties in three energy ranges to unveil the intraband Lifshitz transition. As shown in Figs. 4(e)–4(g), different Fermi surface topologies indeed are observed when the chemical potential  $\mu$  lies in three energy ranges. According to the calculated Fermi surface properties, the energy level V4 is referred to as the first Lifshitz transition point and the energy level Q is referred to as the second Lifshitz transition point. Considering strain-tunable  $E_{V1-V4}$  and  $E_{V4-Q}$ , the intraband Lifshitz transition also should be modulated by external strain. Moreover, the previous study has demonstrated that if the chemical potential  $\mu$  is higher

than the first Lifshitz transition point, the system will have the largest spin-charge conversion conductivity [30].

Aiming to probe the synergic effect of strain and electric field on the intraband Lifshitz transition, the electric-field effect on  $E_{V1-V4}$  and  $E_{V4-Q}$  under four tensile strains is further investigated. As seen in Fig. 5, a perfect linear relation between  $E_{V1-V4}$  and electric field is always observed in all systems no matter how the tensile strain is applied.  $E_{V1-V4}$  decreases linearly with the positive electric field but increases linearly with the negative electric field. The reason why  $E_{V1-V4}$  is linearly dependent on the external electric field can be well explained from the fact that  $E_{V1-V4}$  is original from the Rashba-type spin splitting. It is known that Rashba effect is induced by the symmetry breaking coupling with spin-orbit interaction. Generally speaking, Rashba effect can be tuned linearly by electric field, which has been reported in many 2D Rashba materials [52,59–61]. This brings a linear variation of  $E_{V1-V4}$  with electric field. In contrast, the response of  $E_{V4-Q}$  is different from  $E_{V1-V4}$ . For  $\text{PSi}_2\text{As}$ ,  $E_{V4-Q}$  gradually decreases within the electric field considered under +2% and +3% tensile strains, but it has a minimum under +4% and +5%

tensile strains. For  $\text{PGe}_2\text{As}$  and  $\text{PSn}_2\text{As}$ ,  $E_{V4-Q}$  has a minimum under +2% and +3% tensile strains, but it gradually increases within the electric field considered under +4% and +5% tensile strains. These results clearly suggest the presence of the synergic effect of strain and electric field.

For  $\text{PPb}_2\text{As}$ , a large energy difference between the V1 and V2 energy levels induces the anisotropic sombrero-type VBT and produces multiple intraband Lifshitz transition points (see Fig. S15 [45]). When the chemical potential  $\mu$  shifts from  $\mu_1$  to  $\mu_6$ , the Fermi surface topology changes six times, implying five Lifshitz transition points near the VBT. The remarkable difference between  $\text{PPb}_2\text{As}$  and other systems is attributed to the strong SOC and large atomic radius of the Pb atom. Here, the synergic effect of strain and electric field is not considered since the semiconductor-metal transition is found in  $\text{PPb}_2\text{As}$  by applying small tensile strain.

#### D. Magnetic and electronic transitions of hole-doped $\text{PA}_2\text{As}$

Another important characteristic of the sombrero-type band is the introduction of ferromagnetism and half-metallicity when the hole is injected [9]. Next, we intensively investigate the hole-doping effect on Janus  $\text{PA}_2\text{As}$  monolayers. Although intrinsic Janus  $\text{PA}_2\text{As}$  monolayers are nonmagnetic, they spontaneously become the ferromagnetic state by introducing hole doping. To verify the magnetic properties, we calculate the magnetic moment per hole and magnetic energy per hole based on the spin-polarized density functional theory. The magnetic moment per hole is calculated using the expression [9]  $\sum_{n\mathbf{k}\in\text{hole}} -\langle n\mathbf{k}|\mathbf{m}|n\mathbf{k}\rangle / \sum_{n\mathbf{k}\in\text{hole}} \langle n\mathbf{k}|n\mathbf{k}\rangle$ , where  $\mathbf{m}$  and  $|n\mathbf{k}\rangle$  are the spin magnetic moment operator and Bloch states, respectively. The magnetic energy per hole  $\Delta E_M$  is the total energy difference between the spin-polarization and nonspin-polarization calculations normalized by the number of holes, i.e.,  $\Delta E_M = (E_{\text{spin}} - E_{\text{nonspin}})/N$ , where  $E_{\text{spin}}$  and  $E_{\text{nonspin}}$  are the total energy of the spin-polarization and nonspin-polarization calculations, respectively, and  $N$  is the number of holes. A negative value of  $\Delta E_M$  indicates the preference of ferromagnetic ground state. In our spin-polarization calculations, the direction of magnetic moment is set along the  $\mathbf{z}$  direction.

Figure 6(a) shows the calculated  $\Delta E_M$  as a function of hole carrier density  $p$ . One can find that all Janus  $\text{PA}_2\text{As}$  monolayers produce the ferromagnetic ground state upon hole doping, but  $\Delta E_M$  fluctuates with hole density  $p$ . All systems return to the nonmagnetic ground state once hole density exceeds the critical value. For  $\text{PSi}_2\text{As}$  and  $\text{PGe}_2\text{As}$ , the magnetic ground state only remains in a narrow doping range, i.e.,  $9 \times 10^{13} < p < 15 \times 10^{13} \text{ cm}^{-2}$  and  $6 \times 10^{13} < p < 9 \times 10^{13} \text{ cm}^{-2}$ , respectively. The most stable magnetic ground state emerges at  $p = 12 \times 10^{13} \text{ cm}^{-2}$  for  $\text{PSi}_2\text{As}$  and  $8 \times 10^{13} \text{ cm}^{-2}$  for  $\text{PGe}_2\text{As}$ . Correspondingly, the largest  $\Delta E_M$  is calculated to be 2.55 and 3.02 meV/hole for  $\text{PSi}_2\text{As}$  and  $\text{PGe}_2\text{As}$ , respectively. At the mean field level, the Curie transition temperature  $T_c$  can be approximately estimated through  $T_c = 2\Delta E_M/3k_B$  [62], where  $k_B$  is the Boltzmann constant. The estimated  $T_c$  of  $\text{PSi}_2\text{As}$  and  $\text{PGe}_2\text{As}$  under the most stable magnetic ground state is 19.8 and 23.5 K, respectively. For  $\text{PSn}_2\text{As}$  and  $\text{PPb}_2\text{As}$ , the magnetic ground state emerges in a wide doping range, i.e.,  $1 \times 10^{13} < p < 8 \times 10^{13} \text{ cm}^{-2}$

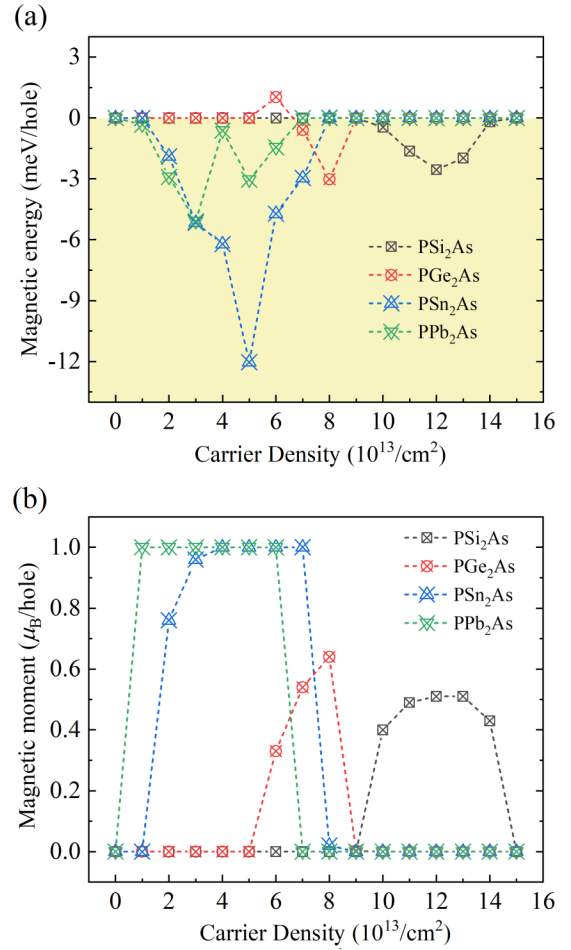


FIG. 6. (a) Magnetic energy per hole and (b) magnetic moment per hole of hope-doped Janus  $\text{PA}_2\text{As}$  monolayers as a function of hole carrier density.

and  $0 < p < 7 \times 10^{13} \text{ cm}^{-2}$ , respectively. We notice that a relatively low hole density can lead to the nonmagnetic to ferromagnetic transition. The most stable magnetic ground state is verified at  $p = 5 \times 10^{13} \text{ cm}^{-2}$  of  $\text{PSn}_2\text{As}$  and  $3 \times 10^{13} \text{ cm}^{-2}$  of  $\text{PPb}_2\text{As}$ , respectively. Correspondingly, the estimated  $T_c$  is 93.5 and 39.5 K, respectively. We notice that the Curie transition temperature  $T_c$  of  $\text{PSn}_2\text{As}$  is comparable to that of hole-doped GaSe [9].

As seen in Fig. 6(b), the trend of the magnetic moment with hole density is evidently distinct from that of the magnetic energy. The nonzero magnetic moment emerges when hole density  $p$  is higher than  $9 \times 10^{13}$  and  $6 \times 10^{13} \text{ cm}^{-2}$  for  $\text{PSi}_2\text{As}$  and  $\text{PGe}_2\text{As}$ , respectively. The magnetic moment increases with hole density and reaches the maximum of 0.51 and 0.64  $\mu_B/\text{hole}$  at  $p = 12 \times 10^{13}$  and  $8 \times 10^{13} \text{ cm}^{-2}$  for  $\text{PSi}_2\text{As}$  and  $\text{PGe}_2\text{As}$ , respectively, and then rapidly returns to zero. Interestingly, a saturated magnetic moment of 1  $\mu_B/\text{hole}$  is reached at  $p = 1 \times 10^{13}$  and  $4 \times 10^{13} \text{ cm}^{-2}$  for  $\text{PSn}_2\text{As}$  and  $\text{PPb}_2\text{As}$ , respectively, which maintains in a relative wide doping range for  $\text{PPb}_2\text{As}$ . The critical hole density to induce ferromagnetic-nonmagnetic transition is at  $p = 9 \times 10^{13}$  and  $7 \times 10^{13} \text{ cm}^{-2}$  for  $\text{PSn}_2\text{As}$  and  $\text{PPb}_2\text{As}$ , respectively. We find that for  $\text{PSn}_2\text{As}$  the magnetic moment



monotonically increases with hole density before the saturation value  $1 \mu_B/\text{hole}$ , whereas for  $\text{PPb}_2\text{As}$  it rapidly reaches the saturation value of  $1 \mu_B/\text{hole}$  even at very low hole density. Similar results were also reported in other hole-doped 2D sombrero-type band materials, such as  $\text{GaO}$  [26],  $\text{InO}$  [26],  $\text{GaSe}$  [9],  $\text{SnO}$  [16,18], blue phosphorene [24],  $\text{InP}_3$  [27] and others.

Apart from presenting the hole density dependence of magnetic moment per hole, we also plot the magnetic moment per cell as a function of hole density (see Fig. S16(a) [45]). An almost linear increment of the magnetic moment with hole density is observed, and then, further increment of hole density leads to ferromagnetic-nonmagnetic transition. These findings are in accordance with the hole-doped multilayer  $\text{GaS}$  and  $\text{GaSe}$  monolayers [25]. Under the most stable magnetic ground state, the spin density of  $\text{PA}_2\text{As}$  is calculated (see Fig. S16(b) [45]). It is found that most of the magnetic states originate from the out of plane orbital, which is in agreement with the previous electronic structure analysis.

The physical origin of magnetism for the hole-doped Janus  $\text{PA}_2\text{As}$  monolayers can be understood from the Stoner criterion [63], i.e.,  $D(E_F)I_S > 1$ , where  $D(E_F)$  is the DOS at the Fermi level with the nonmagnetic state and  $I_S$  is the Stoner parameter. When the Stoner criterion is satisfied, the system would be unstable at the nonmagnetic state. The Stoner ferromagnetic transition can reduce the total energy, and thus the spontaneous magnetization. The Stoner parameter  $I_S$  is calculated through  $I_S = \Delta E_{xc} \mu_B / M_{\text{cell}}$  [64], where  $\Delta E_{xc}$  is the exchange splitting energy near the Fermi level and  $M_{\text{cell}}$  is the magnetic moment per unit cell. Herein we only discuss the Stoner criterion under the most stable magnetic ground state, and the corresponding hole density is at  $p = 12 \times 10^{13}$ ,  $8 \times 10^{13}$ ,  $5 \times 10^{13}$ , and  $3 \times 10^{13} \text{ cm}^{-2}$  for  $\text{PSi}_2\text{As}$ ,  $\text{PGe}_2\text{As}$ ,  $\text{PSn}_2\text{As}$ , and  $\text{PPb}_2\text{As}$ , respectively. Under the most stable magnetic ground state, the calculated  $D(E_F)$  is 4.37, 4.36, 6.21, and 7.66 state/eV, respectively, and the calculated  $I_S$  is 0.74, 0.66, 0.64, and 0.69 eV, respectively. Obviously, the Stoner criterion  $D(E_F)I_S > 1$  is satisfied; thus the spontaneous magnetization happens in the hole-doped Janus  $\text{PA}_2\text{As}$  monolayers. For all reported 2D sombrero-type materials, the physical origin of magnetism upon hole doping has been attributed to the Stoner instability. Because of the experimentally controlled ferromagnetism, we believe that the hole-doped Janus  $\text{PA}_2\text{As}$  monolayers are promising candidates for applying in spintronic devices.

Hole doping not only gives rise to the electronic transition, but also to the nonmagnetic-magnetic transition. Although  $\text{PSi}_2\text{As}$  and  $\text{PGe}_2\text{As}$  are intrinsic semiconductors, they undergo the semiconductor-metal transition upon hole doping (see Fig. S17 [45]). Specifically,  $\text{PSn}_2\text{As}$  undergoes multiple electronic transitions, i.e., semiconductor to metal, metal to half-metal, and half-metal to metal (see Fig. S18 [45]). For  $p < 2 \times 10^{13} \text{ cm}^{-2}$ , the VBT is fully occupied and the system is a nonmagnetic semiconductor. For  $2 \times 10^{13} \leq p \leq 4 \times 10^{13} \text{ cm}^{-2}$ ,  $\text{PSn}_2\text{As}$  becomes a magnetic metal. At  $p = 5 \times 10^{13} \text{ cm}^{-2}$ , the valence band is half filled and the Fermi level only crosses the spin-down channel, rendering the half-metallicity. The electronic spin in this situation allows 100% polarization at the Fermi level, which is an ideal characteristic for spintronic applications. The Fermi level crosses both spin

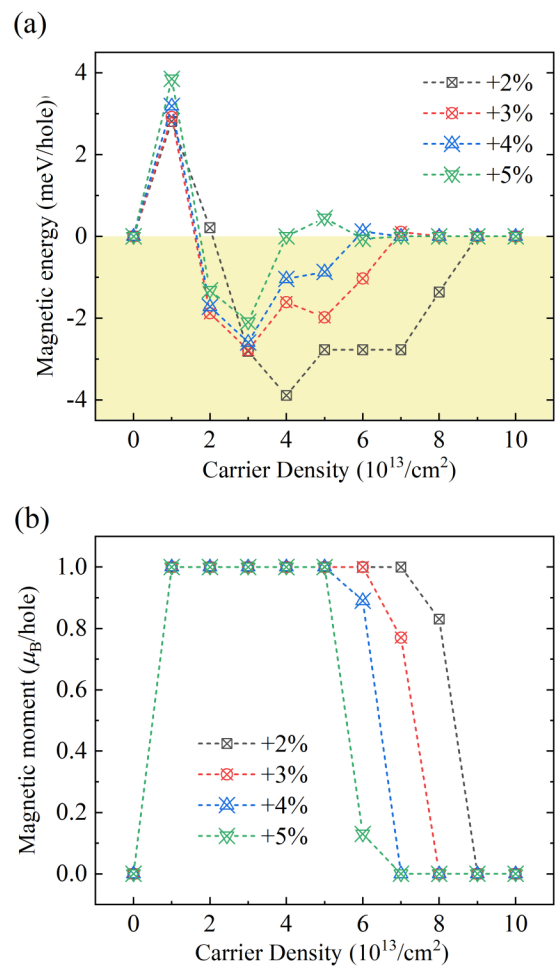


FIG. 7. (a) Magnetic energy and (b) magnetic moment of  $\text{PSi}_2\text{As}$  under different tensile strains as a function of hole density.

channels as a further increment of hole density, rendering the magnetic metallicity. When the hole density is high enough,  $\text{PSn}_2\text{As}$  becomes a nonmagnetic metal. In the case of  $\text{PPb}_2\text{As}$ , a nonmagnetic-magnetic semiconductor transition is induced at low hole density while a semiconductor-metal transition is realized at high hole density (see Fig. S18 [45]).

### E. Strain effect on the electronic and magnetic properties of hole-doped $\text{PA}_2\text{As}$

In order to understand how strain will affect the hole doping induced ferromagnetism, we investigate the strained  $\text{PA}_2\text{As}$  upon hole doping. As suggested in the discussion of the electronic properties, tensile strain modifies the band dispersion near the VBT, which is a key factor in influencing the hole-doping effect. For the sake of brevity, we only discuss the strained  $\text{PSi}_2\text{As}$  monolayer in detail. The results of other monolayers can be found in the Supplemental Material [45]. Figure 7(a) shows the magnetic energy per hole as a function of hole density under four tensile strains. Under the most stable magnetic state, +2%, +3%, and +4% tensile strains enlarge the magnetic energy while +5% tensile strain lowers the magnetic energy, as compared to the strain-free situation [see Fig. 6(a)]. At a certain hole density, the magnetic energy

decreases with tensile strain. This result is contrary to the hole-doped  $\alpha$ -In<sub>2</sub>Se<sub>3</sub> [65], for which the magnetic energy increases with tensile strain. Furthermore, the estimated  $T_c$  under the most stable magnetic state is 30.2, 21.6, 20.1, and 16.2 K for four tensile strains, respectively.

For strained PSi<sub>2</sub>As, a very low hole density can be sufficiently engaged to realize the saturated magnetic moment of  $1 \mu_B/\text{hole}$ , as seen in Fig. 7(b), indicating a strong coupling between tensile strain and magnetism. However, such magnitude of the magnetic moment cannot be obtained in strain-free PSi<sub>2</sub>As at all hole densities considered. A dramatic strain effect of the magnetic state provides the possibility of tuning the magnetism in practical applications. In particular, the plateau region of the  $1 \mu_B/\text{hole}$  is tunable through altering the tensile strain. We find the widest plateau region of  $1 \times 10^{13} \leq p \leq 7 \times 10^{13} \text{ cm}^{-2}$  under +2% tensile strain and the narrowest plateau region of  $1 \times 10^{13} \leq p \leq 5 \times 10^{13} \text{ cm}^{-2}$  under +5% tensile strain, respectively. These results are correlated to the strain-induced modification of the VBT. As shown in Fig. S19 [45], the sombrero strength  $E_0/k_0$  displays a gradual increment with tensile strain, resulting in a reduction of the localization of the DOS. In terms of  $D(E_F) \propto m^{*3/2} \sqrt{E_{\text{VBT}} - E_F}$  [66], ferromagnetism only is maintained with a large effective mass  $m^*$ , which requires a small value of  $E_0/k_0$ . Thus, a wide plateau region is found under small tensile strain. A similar finding was also revealed in GaS and GaSe multilayers [25], in which the magnetic moment decreased with the weakness of the sombrero size.

On the other hand, tensile strain pronouncedly modifies the electronic properties. For strain-free PSi<sub>2</sub>As, it only exhibits the magnetic metallicity during hole doping. For strained PSi<sub>2</sub>As, however, three electronic properties, magnetic semiconductor, half-metallicity, and nonmagnetic metallicity, are revealed with changing the hole density. We can clearly observe these changes from the calculated band structures (see Fig. S20 [45]). At low hole density, the VBT is fully occupied, rendering the semiconducting feature. Further increment of hole density makes the VBT entirely spin polarized. Since the Fermi level only crosses the spin-down channel, the system exhibits half-metallicity. As hole density exceeds the critical value, the Fermi level crosses both spin channels owing to the Rashba effect, rendering the nonmagnetic metallicity. Although both the electronic and magnetic properties are modulated by tensile strain, the magnetic states are still contributed by the out of plane orbital.

Figure 8 plots the hole density dependence of the spin-splitting energy  $\Delta E_{\text{spin}} = E_{\uparrow}(k) - E_{\downarrow}(k)$  under four tensile strains. One can observe that both with and without SOC the “ $\Lambda$ ” type variation is presented, implying the existence of the maximum of the spin-splitting energy. For all strained systems,  $\Delta E_{\text{spin}}$  without SOC is perfectly in line with the magnetic moment per cell as expected. This was also reported in the hole-doped first-row  $d_0$  semiconductors [66]. After the maximum, it sharply descends to zero. In contrast to  $\Delta E_{\text{spin}}$  without SOC,  $\Delta E_{\text{spin}}$  with SOC displays a slight variation at low hole density and a rapid increment at moderate hole density, and finally it returns to a stable value at high hole density. Because of the Rashba effect,  $\Delta E_{\text{spin}}$  with SOC has the same value between the undoped and heavily doped situations. It is interesting that  $\Delta E_{\text{spin}}$  with SOC is nearly unaffected by

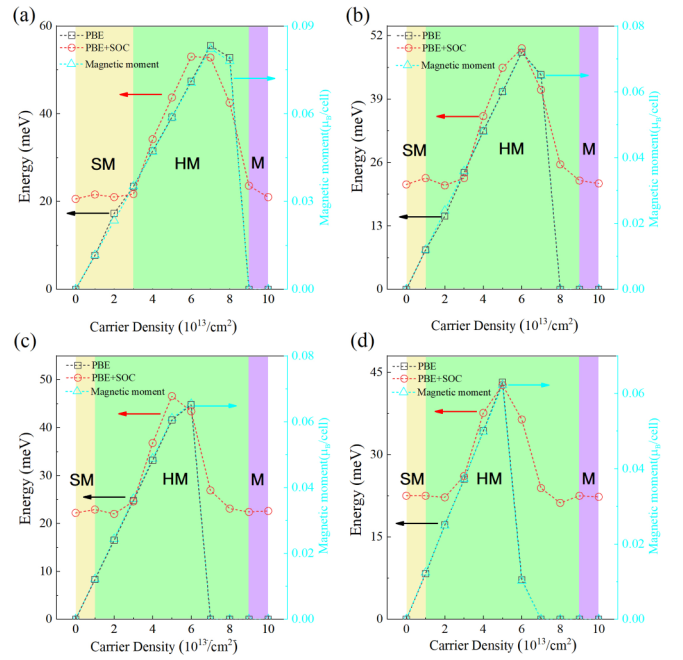


FIG. 8. Spin-splitting energy without and with SOC and magnetic moment of PSi<sub>2</sub>As as a function of hole density under tensile strain (a) +2%, (b) +3%, (c) +4%, and (d) +5%, respectively. SM, HM, and M denote the semiconducting, half-metallic, and metallic features, respectively.

the resultant magnetism at low hole density. These interesting observations can be understood from a competition between the Rashba SOC and the hole doping induced magnetism. Both in the undoped and heavily doped situations, the system is in the nonmagnetic state, and thus the  $\Delta E_{\text{spin}}$  entirely comes from the Rashba SOC. When the hole is at low density, the resultant magnetism is relatively weak and the  $\Delta E_{\text{spin}}$  mainly comes from the Rashba SOC rather than the spin polarization. We can see from Fig. 7(a) that although low hole density (below  $2 \times 10^{13} \text{ cm}^{-2}$ ) induces the magnetism, the ground state of the doped system still is nonmagnetic. This also confirms the weak magnetic effect. When the hole density is high enough, the strong magnetic effect dramatically affects the Rashba SOC and the  $\Delta E_{\text{spin}}$  mainly comes from the spin polarization. For the electronic properties, all systems undergo semiconductor to half-metal and half-metal to metal transitions. Moreover, a wide half-metal region is found under four tensile strains considered.

Finally, the feasibility to realize ferromagnetism through introducing  $p$ -type dopants and defects is explored, as seen in the Supplemental Material [45]. The P and As atoms substituted by the A atoms in a supercell model are used to realize the  $p$ -type doping, and removing one P, As, or A atom is used to realize the monovacancy defect. We find that a stable magnetic moment of  $1 \mu_B/\text{hole}$  is obtained through substitutional doping, the P atoms being replaced by the A atoms. The calculated magnetic energies of  $p$ -type doped PSi<sub>2</sub>As to PPb<sub>2</sub>As are 164.8, 39.6, 13.1, and 5.9 meV/hole, respectively, which are larger than those of the hole doping. Analysis of the spin density indicates that the magnetic states are mainly localized around the dopants in PSi<sub>2</sub>As, PGe<sub>2</sub>As, and PSn<sub>2</sub>As,

but show obvious delocalization in  $\text{PPb}_2\text{As}$ . The  $p$ -type doped  $\text{PPb}_2\text{As}$  and  $\text{PSn}_2\text{As}$  exhibit the half-metallicity, whereas the  $p$ -type doped  $\text{PGe}_2\text{As}$  and  $\text{PSi}_2\text{As}$  exhibit the semiconducting feature. In contrast, the monovacancy defect cannot give rise to ferromagnetism except for the  $\text{PPb}_2\text{As}$ . When forming the P monovacancy in  $\text{PPb}_2\text{As}$ , the system becomes a half-metal with the magnetic moment of  $1 \mu_B$ . Overall, substitutional doping of the P atoms by the A atoms is a more effective way to introduce the ferromagnetism in Janus  $\text{PA}_2\text{As}$  monolayers.

#### IV. CONCLUSION

In summary, we have predicted a class of Janus 2D materials,  $\text{PA}_2\text{As}$  ( $A = \text{Si}, \text{Ge}, \text{Sn}, \text{and Pb}$ ) monolayers, with strain- and electric field tunable electronic properties. Among them, the external strain can lead to semiconductor-metal transition in  $\text{PPb}_2\text{As}$ . There is an intriguing intraband Lifshitz transition in strained  $\text{PA}_2\text{As}$ , which is caused by the sombrero-type VBT coupling with SOC. This intraband Lifshitz transition can be linearly modulated by an electric field. Because of the Van Hove singularity of the DOS,  $\text{PA}_2\text{As}$  monolayers indicate the

Stoner ferromagnetic transition when a hole is injected. We propose that hole density and tensile strain are two effective methods of controlling the Stoner ferromagnetism. Moreover, various electronic transitions are unveiled as introducing hole doping. Our results provide a class of Janus 2D materials for the future electronic and spintronic devices owing to their experimentally controlled intraband Lifshitz transition and Stoner ferromagnetism.

#### ACKNOWLEDGMENTS

This work was supported by National Natural Science Foundation of China (Grant No. 61751405), Major Science and Technology Project of Precious Metal Materials Genetic Engineering in Yunnan Province (Grants No. 2019ZE001-1, No. 202002AB080001, and No. 2018IC058), Program for Yunling Scholars in Yunnan Province, Program for Donglu Scholars in Yunnan University, and Postdoc Science Foundation of Yunnan University. Computational resources were provided by the High Performance Computing Center of Yunnan University.

- 
- [1] A. Chaves, J. G. Azadani, H. Alsaman, D. R. da Costa, R. Frisenda, A. J. Chaves, S. H. Song, Y. D. Kim, D. He, J. Zhou, A. Castellanos-Gomez, F. M. Peeters, Z. Liu, C. L. Hinkle, S.-H. Oh, P. D. Ye, S. J. Koester, Y. H. Lee, P. Avouris, X. Wang *et al.*, Bandgap engineering of two-dimensional semiconductor materials, *npj 2D Mater. Appl.* **4**, 29 (2020).
- [2] N. R. Glavin, R. Rao, V. Varshney, E. Bianco, A. Apte, A. Roy, E. Ringe, and P. M. Ajayan, Emerging applications of elemental 2D materials, *Adv. Mater.* **32**, 1904302 (2020).
- [3] S. Hastrup, M. Strange, M. Pandey, T. Deilmann, P. S. Schmidt, N. F. Hinsche, M. N. Gjerding, D. Torelli, P. M. Larsen, A. C. Riis-Jensen, J. Gath, K. W. Jacobsen, J. J. Mortensen, T. Olsen, and K. S. Thygesen, The computational 2D materials database: High-throughput modeling and discovery of atomically thin crystals, *2D Mater.* **5**, 042002 (2018).
- [4] O. Ü. Aktürk, E. Aktürk, and S. Ciraci, Effects of adatoms and physisorbed molecules on the physical properties of antimonene, *Phys. Rev. B* **93**, 035450 (2016).
- [5] C. Ke, Y. Wu, G.-Y. Guo, W. Lin, Z. Wu, C. Zhou, and J. Kang, Tuning the Electronic, Optical, and Magnetic Properties of Monolayer Gase with a Vertical Electric Field, *Phys. Rev. Appl.* **9**, 044029 (2018).
- [6] Q. Wang, W. Yu, X. Fu, C. Qiao, C. Xia, and Y. Jia, Electronic and magnetic properties of  $\text{SnSe}$  monolayers doped by Ga, In, As, and Sb: A first-principles study, *Phys. Chem. Chem. Phys.* **18**, 8158 (2016).
- [7] S. Oh, J. Y. Lim, S. Im, and H. J. Choi, Stability, efficiency, and mechanism of  $n$ -type doping by hydrogen adatoms in two-dimensional transition metal dichalcogenides, *Phys. Rev. B* **100**, 085416 (2019).
- [8] A. Bafekry, S. F. Shayesteh, and F. M. Peeters,  $\text{C}_3\text{N}$  monolayer: Exploring the emerging of novel electronic and magnetic properties with adatom adsorption, functionalizations, electric field, charging, and strain, *J. Phys. Chem. C* **123**, 12485 (2019).
- [9] T. Cao, Z. Li, and S. G. Louie, Tunable Magnetism and Half-Metallicity in Hole-Doped Monolayer  $\text{GaSe}$ , *Phys. Rev. Lett.* **114**, 236602 (2015).
- [10] Y. Kadioglu, S. B. Kilic, S. Demirci, O. Ü. Aktürk, E. Aktürk, and S. Ciraci, Modification of electronic structure, magnetic structure, and topological phase of bismuthene by point defects, *Phys. Rev. B* **96**, 245424 (2017).
- [11] X. Lin and J. Ni, Much stronger binding of metal adatoms to silicene than to graphene: A first-principles study, *Phys. Rev. B* **86**, 075440 (2012).
- [12] H. Zhang, C. Lazo, S. Blugel, S. Heinze, and Y. Mokrousov, Electrically Tunable Quantum Anomalous Hall Effect in Graphene Decorated by  $5d$  Transition-Metal Adatoms, *Phys. Rev. Lett.* **108**, 056802 (2012).
- [13] Y. Liu, T. Wang, J. Robertson, J. Luo, Y. Guo, and D. Liu, Band structure, band offsets, and intrinsic defect properties of few-layer arsenic and antimony, *J. Phys. Chem. C* **124**, 7441 (2020).
- [14] G. Yu, M. Zhu, and Y. Zheng, First-principles study of  $3d$  transition metal atom adsorption onto graphene: The role of the extended line defect, *J. Mater. Chem. C* **2**, 9767 (2014).
- [15] O. V. Yazyev, Magnetism in Disordered Graphene and Irradiated Graphite, *Phys. Rev. Lett.* **101**, 037203 (2008).
- [16] L. Seixas, A. S. Rodin, A. Carvalho, and A. H. Castro Neto, Multiferroic Two-Dimensional Materials, *Phys. Rev. Lett.* **116**, 206803 (2016).
- [17] K. Iordanidou, M. Houssa, J. Kioseoglou, V. V. Afanas'ev, A. Stesmans, and C. Persson, Hole-doped 2D  $\text{InSe}$  for spintronic applications, *ACS Appl. Nano Mater.* **1**, 6656 (2018).
- [18] L. Guan and J. Tao, Mechanism of Magnetic Coupling in Carrier-Doped  $\text{SnO}$  Nanosheets, *Phys. Rev. Appl.* **8**, 064019 (2017).
- [19] Y. Nie, M. Rahman, P. Liu, A. Sidike, Q. Xia, and G.-h. Guo, Room-temperature half-metallicity in monolayer honeycomb structures of group-V binary compounds with carrier doping, *Phys. Rev. B* **96**, 075401 (2017).
- [20] N. F. Q. Yuan, H. Isobe, and L. Fu, Magic of high-order Van Hove singularity, *Nat. Commun.* **10**, 5769 (2019).
- [21] X.-T. Jin, X.-W. Yan, and M. Gao, First-principles calculations of monolayer hexagonal boron nitride: Possibility of superconductivity, *Phys. Rev. B* **101**, 134518 (2020).

- [22] H. Banerjee, P. Barone, and S. Picozzi, Half-metallic ferromagnetism in layered CdOHCl induced by hole doping, *2D Mater.* **8**, 025027 (2021).
- [23] W. Feng, G.-Y. Guo, and Y. Yao, Tunable magneto-optical effects in hole-doped group-IIIa metal-monochalcogenide monolayers, *2D Mater.* **4**, 015017 (2016).
- [24] B. Fu, W. Feng, X. Zhou, and Y. Yao, Effects of hole doping and strain on magnetism in buckled phosphorene and arsenene, *2D Mater.* **4**, 025107 (2017).
- [25] F. Li, X. Zhou, W. Feng, B. Fu, and Y. Yao, Thickness-dependent magneto-optical effects in hole-doped GaS and GaSe multilayers: A first-principles study, *New J. Phys.* **20**, 043048 (2018).
- [26] S. Demirci, N. Avazli, E. Durgun, and S. Cahangirov, Structural and electronic properties of monolayer group III monochalcogenides, *Phys. Rev. B* **95**, 115409 (2017).
- [27] N. Miao, B. Xu, N. C. Bristowe, J. Zhou, and Z. Sun, Tunable magnetism and extraordinary sunlight absorbance in indium triphosphide monolayer, *J. Am. Chem. Soc.* **139**, 11125 (2017).
- [28] D. K. Efetov and P. Kim, Controlling Electron-Phonon Interactions in Graphene at Ultrahigh Carrier Densities, *Phys. Rev. Lett.* **105**, 256805 (2010).
- [29] Y. J. Zhang, T. Oka, R. Suzuki, J. T. Ye, and Y. Iwasa, Electrically switchable chiral light-emitting transistor, *Science* **344**, 725 (2014).
- [30] M. Zhou, D. Zhang, S. Yu, Z. Huang, Y. Chen, W. Yang, and K. Chang, Spin-charge conversion in InSe bilayers, *Phys. Rev. B* **99**, 155402 (2019).
- [31] M.-Y. Liu, L. Gong, Y. He, and C. Cao, Tuning Rashba effect, band inversion, and spin-charge conversion of Janus  $XSn_2Y$  monolayers via an external field, *Phys. Rev. B* **103**, 075421 (2021).
- [32] B. Özdamar, G. Özbal, M. N. Çınar, K. Sevim, G. Kurt, B. Kaya, and H. Sevinçli, Structural, vibrational, and electronic properties of single-layer hexagonal crystals, *Phys. Rev. B* **98**, 045431 (2018).
- [33] S. Lee and Y. K. Kwon, Versatile physical properties of a novel two dimensional materials composed of group IV-V elements, [arXiv:2007.05137v1](https://arxiv.org/abs/2007.05137v1).
- [34] M.-Y. Liu, L. Gong, W.-Z. Li, M.-L. Zhang, Y. He, and C. Cao, Band engineering of  $XBi$  ( $X = Si, Ge, Sn, \text{ and } Pb$ ) single layers via strain and surface chemical-modulation, *Appl. Surf. Sci.* **540**, 148268 (2021).
- [35] G. Kresse and J. Furthmüller, Efficient iterative schemes for *ab initio* total-energy calculations using a plane-wave basis set, *Phys. Rev. B* **54**, 11169 (1996).
- [36] P. E. Blochl, Projector augmented-wave method, *Phys. Rev. B* **50**, 17953 (1994).
- [37] J. P. Perdew, K. Burke, and M. Ernzerhof, Generalized Gradient Approximation Made Simple, *Phys. Rev. Lett.* **77**, 3865 (1996).
- [38] J. Heyd, G. E. Scuseria, and M. Ernzerhof, Hybrid functionals based on a screened Coulomb potential, *J. Chem. Phys.* **118**, 8207 (2003).
- [39] P. Giannozzi, S. Baroni, N. Bonini, M. Calandra, R. Car, C. Cavazzoni, D. Ceresoli, G. L. Chiarotti, M. Cococcioni, I. Dabo, A. Dal Corso, S. de Gironcoli, S. Fabris, G. Fratesi, R. Gebauer, U. Gerstmann, C. Gougoussis, A. Kokalj, M. Lazzeri, L. Martin-Samos *et al.*, QUANTUM ESPRESSO: A modular and open-source software project for quantum simulations of materials, *J. Phys.: Condens. Matter* **21**, 395502 (2009).
- [40] V. Wang, N. Xu, J. C. Liu, G. Tang, and W.-T. Geng, VASPKIT: A user-friendly interface facilitating high-throughput computing and analysis using VASP code, *Comput. Phys. Commun.* **267**, 108033 (2021).
- [41] W. Tang, E. Sanville, and G. Henkelman, A grid-based Bader analysis algorithm without lattice bias, *J. Phys.: Condens. Matter.* **21**, 084204 (2009).
- [42] Q. Wu, S. Zhang, H.-F. Song, M. Troyer, and A. A. Soluyanov, WANNIERTOOLS: An open-source software package for novel topological materials, *Comput. Phys. Commun.* **224**, 405 (2018).
- [43] N. Marzari, A. A. Mostofi, J. R. Yates, I. Souza, and D. Vanderbilt, Maximally localized Wannier functions: Theory and applications, *Rev. Mod. Phys.* **84**, 1419 (2012).
- [44] A. A. Mostofi, J. R. Yates, Y.-S. Lee, I. Souza, D. Vanderbilt, and N. Marzari, WANNIER90: A tool for obtaining maximally-localised Wannier functions, *Comput. Phys. Commun.* **178**, 685 (2008).
- [45] See Supplemental Material at <http://link.aps.org/supplemental/10.1103/PhysRevB.104.035409> for details of the structural properties, electronic properties, and hole-doping effect of Janus  $PA_2As$  monolayers.
- [46] M. K. Mohanta, A. Rawat, N. Jena, R. Ahammed, and A. De Sarkar, Superhigh flexibility and out-of-plane piezoelectricity together with strong anharmonic phonon scattering induced extremely low lattice thermal conductivity in hexagonal buckled  $CdX$  ( $X = S, Se$ ) monolayers, *J. Phys.: Condens. Matter.* **32**, 355301 (2020).
- [47] M. K. Mohanta and A. De Sarkar, Coupled spin and valley polarization in monolayer  $HfN_2$  and valley-contrasting physics at the  $HfN_2 - WSe_2$  interface, *Phys. Rev. B* **102**, 125414 (2020).
- [48] M. Yagmurcukardes, R. T. Senger, and F. M. Peeters, and H. Sahin, Mechanical properties of monolayer GaS and GaSe crystals, *Phys. Rev. B* **94**, 245407 (2016).
- [49] M. Demirtas, M. J. Varjovi, M. M. Cicek, and E. Durgun, Tuning structural and electronic properties of two-dimensional aluminum monochalcogenides: Prediction of Janus  $Al_2XX'(X/X': O, S, Se, Te)$  monolayers, *Phys. Rev. Mater.* **4**, 114003 (2020).
- [50] S. B. Touski and N. Ghobadi, Structural, electrical, and Rashba properties of monolayer Janus  $Si_2XY$  ( $X, Y = P, As, Sb, \text{ and } Bi$ ), *Phys. Rev. B* **103**, 165404 (2021).
- [51] F. Ersan and C. Ataca, Janus  $PtX_nY_{2-n}$  ( $X, Y = S, Se, Te; 0 \leq n \leq 2$ ) Monolayers for Enhanced Photocatalytic Water Splitting, *Phys. Rev. Appl.* **13**, 064008 (2020).
- [52] Q.-F. Yao, J. Cai, W.-Y. Tong, S.-J. Gong, J.-Q. Wang, X. Wan, C.-G. Duan, and J. H. Chu, Manipulation of the large Rashba spin splitting in polar two-dimensional transition-metal dichalcogenides, *Phys. Rev. B* **95**, 165401 (2017).
- [53] L. Zhang, Z. Yang, T. Gong, R. Pan, H. Wang, Z. Guo, H. Zhang, and X. Fu, Recent advances in emerging Janus two-dimensional materials: From fundamental physics to device applications, *J. Mater. Chem. A* **8**, 8813 (2020).
- [54] A. Kandemir and H. Sahin, Janus single layers of  $In_2SSe$ : A first-principles study, *Phys. Rev. B* **97**, 155410 (2018).
- [55] Z. Guo, X. Hao, J. Dong, H. Li, Y. Gong, D. Yang, J. Liao, S. Chu, Y. Li, X. Li, and D. Chen, Prediction of topological non-trivial semimetals and pressure-induced Lifshitz transition in  $1T'-MoS_2$  layered bulk polytypes, *Nanoscale* **12**, 22710 (2020).



- [56] H. Jiang, L. Li, J. Gong, and S. Chen, Characterization of Lifshitz transitions in topological nodal line semimetals, *Eur. Phys. J. B* **91**, 75 (2018).
- [57] D. Novko, Broken adiabaticity induced by Lifshitz transition in MoS<sub>2</sub> and WS<sub>2</sub> single layers, *Commun. Phys.* **3**, 30 (2020).
- [58] S. L. Skornyakov and I. Leonov, Correlated electronic structure, orbital-dependent correlations, and Lifshitz transition in tetragonal FeS, *Phys. Rev. B* **100**, 235123 (2019).
- [59] T. Hu, F. Jia, G. Zhao, J. Wu, A. Stroppa, and W. Ren, Intrinsic and anisotropic Rashba spin splitting in Janus transition-metal dichalcogenide monolayers, *Phys. Rev. B* **97**, 235404 (2018).
- [60] W. Ju, D. Wang, T. Li, Y. Zhang, Z. Gao, L. Ren, H. Li, and S. Gong, Remarkable Rashba spin splitting induced by an asymmetrical internal electric field in polar III-VI chalcogenides, *Phys. Chem. Chem. Phys.* **22**, 9148 (2020).
- [61] C. Liu, H. Gao, Y. Li, K. Wang, L. A. Burton, and W. Ren, Manipulation of the Rashba effect in layered tellurides *MTe* ( $M = \text{Ge, Sn, Pb}$ ), *J. Mater. Chem. C* **8**, 5143 (2020).
- [62] A. Albar and U. Schwingenschlögl, Magnetism in 3*d* transition metal doped SnO, *J. Mater. Chem. C* **4**, 8947 (2016).
- [63] P. M. Marcus and V. L. Moruzzi, Stoner model of ferromagnetism and total-energy band theory, *Phys. Rev. B* **38**, 6949 (1988).
- [64] M. Hortamani, L. Sandratskii, P. Kratzer, I. Mertig, and M. Scheffler, Exchange interactions and critical temperature of bulk and thin films of MnSi: A density functional theory study, *Phys. Rev. B* **78**, 104402 (2008).
- [65] C. Liu, B. Wang, G. Jia, P. Liu, H. Yin, S. Guan, and Z. Cheng, Tunable magnetism in ferroelectric  $\alpha$ -In<sub>2</sub>Se<sub>3</sub> by hole-doping, *Appl. Phys. Lett.* **118**, 072902 (2021).
- [66] H. Peng, H. J. Xiang, S. H. Wei, S. S. Li, J. B. Xia, and J. Li, Origin and Enhancement of Hole-Induced Ferromagnetism in First-Row *d*<sub>0</sub> Semiconductors, *Phys. Rev. Lett.* **102**, 017201 (2009).